

L-Band Passive and Active Microwave Geophysical Model Functions of Ocean Surface Winds and Applications to Aquarius Retrieval

Simon H. Yueh, *Fellow, IEEE*, Wenqing Tang, Alexander G. Fore, Gregory Neumann, Akiko Hayashi, Adam Freedman, Julian Chaubell, and Gary S. E. Lagerloef

Abstract—The L-band passive and active microwave geophysical model functions (GMFs) of ocean surface winds from the Aquarius data are derived. The matchups of Aquarius data with the Special Sensor Microwave Imager (SSM/I) and National Centers for Environmental Prediction (NCEP) winds were performed and were binned as a function of wind speed and direction. The radar HH GMF is in good agreement with the PALSAR GMF. For wind speeds above $10 \text{ m} \cdot \text{s}^{-1}$, the L-band ocean backscatter shows positive upwind-crosswind (UC) asymmetry; however, the UC asymmetry becomes negative between about 3 and $8 \text{ m} \cdot \text{s}^{-1}$. The negative UC (NUC) asymmetry has not been observed in higher frequency (above C-band) GMFs for ASCAT or QuikSCAT. Unexpectedly, the NUC symmetry also appears in the L-band radiometer data. We find direction dependence in the Aquarius T_{BV} , T_{BH} , and third Stokes data with peak-to-peak modulations increasing from about a few tenths to 2 K in the range of $10\text{--}25\text{-m} \cdot \text{s}^{-1}$ wind speed. The validity of the GMFs is tested through application to wind and salinity retrieval from Aquarius data using the combined active-passive algorithm. Error assessment using the triple collocation analyses of SSM/I, NCEP, and Aquarius winds indicates that the retrieved Aquarius wind speed accuracy is excellent, with a random error of about $0.75 \text{ m} \cdot \text{s}^{-1}$. The wind direction retrievals also appear reasonable and accurate above $10 \text{ m} \cdot \text{s}^{-1}$. The results of the error analysis indicate that the uncertainty of the GMFs for the wind speed correction of vertically polarized brightness temperatures is about 0.14 K for wind speed up to $10 \text{ m} \cdot \text{s}^{-1}$.

Index Terms—Microwave remote sensing, ocean wind, radar, radiometer.

I. INTRODUCTION

L-BAND microwave remote sensing will play an increasingly important role for the global observation of ocean surfaces. Several L-band microwave radiometer and radar missions have been or will be operating in space for land and ocean observations. These include the European Soil Moisture and Ocean Salinity (SMOS) mission [1], the Aquarius/SAC-D mission [2], the Soil Moisture Active–Passive (SMAP) mission [3],

and the Japanese Phased Array type L-band Synthetic Aperture Radar (PALSAR) and its follow-on [4]. The Aquarius and SMAP missions both utilize combined passive/active L-band instruments. Aquarius' passive/active L-band microwave sensor has been designed to map the ocean surface salinity field from space [2]. SMAP's primary objectives are to retrieve soil moisture and detect freeze/thaw, but it will operate continuously over the ocean, and hence, it will have significant potential for ocean surface research.

The measurement principle for salinity remote sensing is based on the response of the L-band (1.413 GHz) sea surface brightness temperatures (T_B) to sea surface salinity (SSS) [5]. To achieve the required 0.2 practical salinity unit (psu) accuracy, the impact of sea surface roughness (e.g., wind-generated ripples, foam, and swell) on the observed brightness temperature has to be accurately corrected, ideally to better than one tenth of a degree kelvin. The influence of wind speed on L-band T_B has been shown by many field studies to be about $0.2\text{--}0.3 \text{ K} \cdot \text{m} \cdot \text{s}^{-1}$ change in wind speed [6]–[11]. Recent analyses of the SMOS data have led to significant improvement in the parameterization of wind speed effects on ocean surface emissivity [12], [13].

However, the relatively large noise equivalent delta T (NEDT) in the SMOS data has not yet allowed an assessment of the wind direction impact on the sea surface brightness temperatures. Recent aircraft campaign data [11] showed that the ocean surface wind direction will modulate the L-band microwave brightness temperatures by 0.5 K or more for wind speed greater than $10 \text{ m} \cdot \text{s}^{-1}$. The wind direction effects will introduce significant errors for salinity retrieval if uncorrected. For example, a directional variation of 0.7 K will result in a salinity retrieval error of about 1 psu for warm waters at 25°C . Here, we have used the Aquarius data to improve the characterization of wind direction effects on vertically and horizontally polarized brightness temperatures T_{BV} and T_{BH} for $0\text{--}20\text{-m} \cdot \text{s}^{-1}$ wind speeds.

Another element of interest is the third Stokes parameter (U) of the passive microwave emission from ocean surfaces. Many aircraft polarimetric radiometers and the WindSat radiometers operating at frequencies above 10 GHz have shown as large as a few kelvin wind direction modulation in the third Stokes parameter data [14]–[17], which have been exploited for wind direction retrieval from the WindSat data [18]. In addition, the third Stokes parameter at L-band, sensitive to polarization

Manuscript received June 19, 2012; revised February 6, 2013; accepted May 17, 2013. Date of publication July 9, 2013; date of current version August 30, 2013.

S. H. Yueh, W. Tang, A. G. Fore, G. Neumann, A. Hayashi, A. Freedman, and J. Chaubell are with the Jet Propulsion Laboratory, California Institute of Technology, Pasadena, CA 91109 USA (e-mail: simon.yueh@jpl.nasa.gov).

G. S. E. Lagerloef is with Earth and Space Research, Seattle, WA 98121 USA.

Color versions of one or more of the figures in this paper are available online at <http://ieeexplore.ieee.org>.

Digital Object Identifier 10.1109/TGRS.2013.2266915

rotation, can be used to retrieve the Faraday rotation angle [19], under the assumption that U emission at the sea surface is zero for all sea states. However, to the best of our knowledge, there have been no clear experimental indications regarding the amplitude of U at L-band frequencies. Therefore, in this paper, we also analyze the Aquarius U data to assess their wind speed and direction dependence.

Ocean wind direction effects have been observed in L-band PALSAR HH data and PALS aircraft campaign data for high winds ($> 10 \text{ m} \cdot \text{s}^{-1}$) [11]. Although the direction signal in the L-band radar backscatter is small for low to mid-range of wind speeds ($< 8 \text{ m} \cdot \text{s}^{-1}$), there are directional variations of a few decibels for $15\text{--}25\text{-m} \cdot \text{s}^{-1}$ wind speeds. We used the Aquarius data to generate the geophysical model function (GMF) model for VV in addition to the improvement for HH polarization.

In Section II, we examine the characteristics of Aquarius matchup data with winds from the Special Sensor Microwave Imager (SSM/I) and the National Centers for Environmental Prediction (NCEP) product. Section III describes the GMFs of various polarization channels for radiometer and radar. Section IV describes the testing and error analyses of the GMFs through applications of the GMFs to wind and salinity retrieval from Aquarius data. Section V provides a summary of the results.

II. MATCHUP OF AQUARIUS DATA WITH OCEAN WIND VECTOR

The Aquarius radiometer and scatterometer have been fully operating since August 25, 2011. Other than interruptions caused by a few spacecraft maneuvers, the data acquisition has been continuous. The Aquarius instrument has three antenna beams, operating at about 29° , 38° , and 46° incidence angles [20]. Each antenna beam has one radiometer (1.413 GHz), which measures the first three Stokes parameters of microwave radiation. The antenna feeds are shared with the scatterometer (1.26 GHz), which acquires the normalized radar cross sections (σ_0) for co- and cross-polarizations.

To assess the response of L-band brightness temperatures and radar σ_0 to ocean surface winds, we analyzed the matchup data set of the Aquarius data with SSM/I F17 wind speed and rain rate [21] and wind vectors from NCEP [22]. The SSM/I F17 and Aquarius data acquired within 1 h from each other are collocated. The SSM/I F17 retrievals are reported on 0.25° latitude and longitude grids. Because the Aquarius footprint size is about 100 km, we average all the SSM/I data grids within 25 km of the center of the Aquarius footprint. The matchup data set covers the time period from August 24, 2011, to April 9, 2012. We have also derived the GMFs using about three months or one year of data. The results are essentially the same at wind speeds below 15 m/s. More data mostly only reduce the scatter at high wind speeds.

The matchup of NCEP winds and Aquarius data has been routinely performed by the Aquarius Data Processing System (ADPS). The NCEP winds are reported every 6 h on 1° grid resolutions and are linearly interpolated in time and bilinearly interpolated in space to match up with the Aquarius observations. In addition to the NCEP winds, ADPS has been matching

up the Reynolds sea surface temperature (SST) [23] and the HYbrid Coordinate Ocean Model (HYCOM) SSS [24], which, along with the NCEP wind matchups, are available in the Aquarius L2 files.

To minimize the effects of rain, we excluded any matchups with nonzero SSM/I rain rate from the data analysis. The rain-free matchups were grouped into bins with step size of $1 \text{ m} \cdot \text{s}^{-1}$ in wind speed and 10° in wind direction. The Aquarius data in each bin were averaged to represent the expected microwave response at the given wind speed and direction.

The matchup and binning approach indicated previously has been used to develop the GMF for spaceborne scatterometer missions, such as QuikSCAT [25] and ASCAT [26]. One critical factor is the choice of the ancillary wind product for matchup. For example, NCEP winds were used for the development of the QuikSCAT GMF, while the European Center for Medium-Range Forecast (ECMWF) was used for ASCAT. There are systematic differences between these types of winds. Our analysis has been performed using two combinations of matchups to test the sensitivity and consistency: 1) SSM/I wind speed and NCEP wind direction and 2) NCEP wind speed and direction. Note that NCEP wind is a meteorological wind, while SSM/I's wind is a microwave remote sensing wind, which is expected to be a better representation of ocean surface roughness than NCEP.

Fig. 1 illustrates the VV and HH radar backscatter versus the relative wind direction for 5-, 8-, 10-, 12-, 15-, and $20\text{-m} \cdot \text{s}^{-1}$ SSM/I wind speeds. Each wind speed panel has three rows for the three antenna beams. There is a clear wind direction dependence in the radar σ_0 s for both polarizations at all wind speeds. The peak-to-peak variations are about 4 dB peak-to-peak at $20 \text{ m} \cdot \text{s}^{-1}$, which agree very well with the aircraft observations [11]. However, the directional signals at $5\text{-m} \cdot \text{s}^{-1}$ wind speed with a peak-to-peak amplitude of 0.7 dB have a negative upwind-crosswind (NUC) asymmetry with σ_0 s at crosswind (90° and 270°) larger than that at upwind (0°) or downwind (180°), while the UC asymmetry is positive at above $10\text{-m} \cdot \text{s}^{-1}$ wind speeds. This feature was seen in the PALSAR HH data but now also confirmed for the VV polarization. A close inspection of the data from 5 to $10 \text{ m} \cdot \text{s}^{-1}$ indicates that the upwind and downwind σ_0 s grow with wind speed, while the crosswind σ_0 s appears to decrease. The beam 2 and beam 3 VV data at $8\text{-m} \cdot \text{s}^{-1}$ wind speed, in fact, feature four peaks with two small peaks at upwind and downwind in addition to the two small peaks at the crosswind directions. This is also barely visible on beam 3 at $5 \text{ m} \cdot \text{s}^{-1}$.

The Bragg scattering mechanism used in two-scale sea surface scattering models [27], [28] is known to produce a positive UC asymmetry—different from the observed L-band radar signals near $5 \text{ m} \cdot \text{s}^{-1}$. The NUC asymmetry (NUC) present in the L-band radar data at around $5\text{-m} \cdot \text{s}^{-1}$ wind speed is likely the result of a scattering mechanism that is different from Bragg and unknown at this time. If there is indeed a different scattering mechanism, the Aquarius data indicate that this NUC scattering mechanism dominates at low winds, while Bragg scattering dominates at high winds. When the wind speed increases from 5 to $10 \text{ m} \cdot \text{s}^{-1}$, the contribution of the NUC scattering mechanism appears to

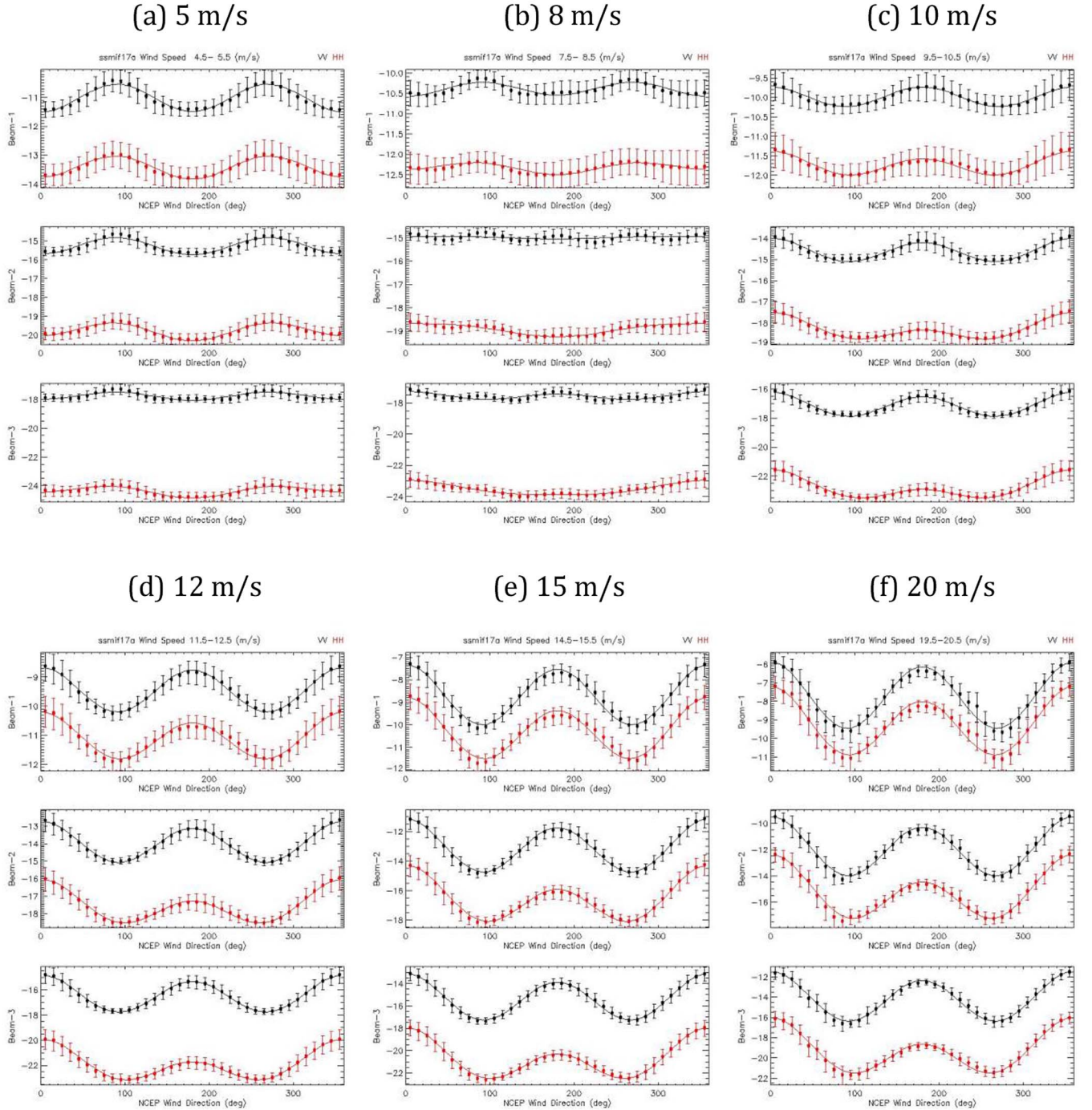


Fig. 1. Aquarius radar backscatter versus NCEP wind direction for six SSM/I wind speeds. In each wind speed panel, the upper row is for beam 1, the middle row is for beam 2, and the bottom row is for beam 3. Black and red dots are the binned matchup averages; vertical bars indicate ± 1 SD. Black and red curves are the three-term cosine series fit for VV and HH, respectively. (a) 5 m/s. (b) 8 m/s. (c) 10 m/s. (d) 12 m/s. (e) 15 m/s. (f) 20 m/s.

decrease, while the Bragg scattering contribution appears to increase.

For the analysis of Aquarius radiometer data, we have considered the effects of Faraday rotation, particularly for the third Stokes parameter. The Aquarius radiometers make partially polarimetric measurements to obtain the first three Stokes parameters, namely, I , Q , and U [29]. I and Q correspond to the sum and difference of the vertically polarized brightness temperature (T_{BV}) and horizontally polarized brightness temperature (T_{BH}). T_{BV} and T_{BH} are measures of the power of

the vertically polarized electrical field (E_V) and horizontally polarized electric field (E_H), while the third and fourth Stokes parameters (U and V) signify the real and imaginary parts of the correlation between E_V and E_H

$$\begin{bmatrix} I \\ Q \\ U \\ V \end{bmatrix} = \begin{bmatrix} T_{BV} + T_{BH} \\ T_{BV} - T_{BH} \\ U \\ V \end{bmatrix} \propto \begin{bmatrix} \langle |E_V|^2 \rangle + \langle |E_H|^2 \rangle \\ \langle |E_V|^2 \rangle - \langle |E_H|^2 \rangle \\ 2\text{Re} \langle E_V E_H^* \rangle \\ 2\text{Im} \langle E_V E_H^* \rangle \end{bmatrix}. \quad (1)$$

The angular brackets denote the ensemble average of the enclosed quantities. Aquarius does not measure the fourth Stokes parameter V .

It is straightforward to show that the first three Stokes parameters from the surface and the ones from the top of the ionosphere, denoted with the subscript “a,” are related to the Faraday rotation angle (Ω) by the following equations for Aquarius:

$$I = I_a \quad (2)$$

$$Q = Q_a \cos(2\Omega) - U_a \sin(2\Omega) \quad (3)$$

$$U = Q_a \sin(2\Omega) + U_a \cos(2\Omega). \quad (4)$$

Equations (3) and (4) are essentially the same as in [19, eqs. (9) and (10)].

Aquarius operates in a sun-synchronous orbit with ascending equator crossing at 6 P.M. The Faraday rotation angle for this dawn/dusk orbit is, in general, quite small, mostly less than 5° , and its impact on T_{BV} and T_{BH} is a few tenths of a kelvin or less. In the standard ADPS processing, the Faraday rotation angle is computed from Q_a and U_a under the assumption that the third Stokes parameter (U) of ocean surface emission is zero [19]. In the Aquarius Level-2 (L2) data files, T_{BV} and T_{BH} are the brightness temperatures at the surface with the Faraday rotation corrected under the assumption of zero for U .

Because we are examining the amplitude of U versus wind speed and direction, we do not apply the assumption $U = 0$ and associated standard ADPS corrections to T_{BV} and T_{BH} in this data analysis. Instead, we use the global International GNSS Service (IGS) Total Electron Content (TEC) product in IONosphere map EXchange (IONEX) format [30] and the International Geomagnetic Reference Field [31] to make an independent estimate of the Faraday rotation angle for each Aquarius observation. Because the IGS-IONEX TEC products are derived from data acquired using GPS satellites operating at a higher altitude than Aquarius', only about 75% of TEC occurs under the Aquarius altitude; this reduced value is used for the estimate of Ω . After the Stokes parameters of the surface emission are computed using (2)–(4) with the rotation angle estimated from IGS-IONEX TEC, the brightness temperatures of vertical and horizontal polarizations can be obtained by

$$T_{BV} = (I + Q)/2 \quad (5)$$

$$T_{BH} = (I - Q)/2. \quad (6)$$

Unlike the radar data, we bin the excess surface emissivity (Δe) by wind speed and direction, rather than the excess surface T_B :

$$\Delta e_p = \frac{T_{Bp} - T_{Bpflat}(SST, SSS, \theta)}{SST}. \quad (7)$$

T_{Bpflat} is the brightness temperature for flat water surfaces computed using the water dielectric constant model [32] for a given Reynolds SST and HYCOM SSS [24]. The subscript “p” stands for the polarization.

The directional features in excess surface emissivity are depicted for several wind speeds in Fig. 2. The peak-to-peak Δe is about 0.0005 at $5\text{ m} \cdot \text{s}^{-1}$ wind speed and rises to about 0.003 at $15\text{ m} \cdot \text{s}^{-1}$. Note that the excess surface emissivity

of 0.003 corresponds to about 1 K in brightness temperature. The directional features above $10\text{ m} \cdot \text{s}^{-1}$ are very similar to those above X-band frequencies [14]–[17]: The horizontal polarization has smaller emissivity at upwind and downwind directions than crosswind, while the vertical polarization exhibits opposite phase signatures. However, like the radar signatures, the phase signature of the horizontally polarized Δe at $5\text{ m} \cdot \text{s}^{-1}$ is opposite to that at above $10\text{ m} \cdot \text{s}^{-1}$ wind speeds. It appears that the NUC scattering mechanism, which drives the UC phase change of active microwave backscatter, is also playing an important role in determining the directional signatures of passive microwave emission.

The directional signals in the third Stokes parameter of sea surface emissions are illustrated in Fig. 3. Because Faraday rotation has a much larger impact on U than T_{BV} and T_{BH} , the error in the estimates of Faraday rotation angle using the IGS-IONEX TEC will result in a relatively larger residual uncertainty in the corrected third Stokes. At $5\text{ m} \cdot \text{s}^{-1}$ wind speed, it seems that there could be a sinusoidal directional dependence in the data for beams 1 and 2, but the amplitude is extremely small, only about 0.0004 peak-to-peak for excess surface emissivity (or 0.1–0.2 K). There is no consistent wind direction dependence at $8\text{ m} \cdot \text{s}^{-1}$, which approximately corresponds to the transition speed of two different opposite UC phase signals observed in the copolarized backscatter data and T_B (Figs. 1 and 2). If we assume that the peak-to-peak variations at $8\text{ m} \cdot \text{s}^{-1}$ are caused entirely by the error of the IGS-IONEX/TEC-derived Faraday rotation correction and matchup process for the third Stokes, then the worst-case error in the corrected U data will be about 0.1 K for beam 1 and as large as 0.5 K for beam 3.

The directional signals in U appear to be robust at 12-, 15-, and $20\text{ m} \cdot \text{s}^{-1}$ wind speeds with peak-to-peak Δe of about 0.002–0.007, corresponding to about 0.6–2 K. The apparent directional modulation is near zero at upwind, crosswind, and downwind directions and peaks at about 45° away from upwind or downwind. This directional dependence at L-band is strikingly similar to that of the higher frequency observations made by aircraft and spaceborne WindSat radiometers [14]–[18].

III. L-BAND GMF

The matchup data using either SSM/I or NCEP wind for binning have been used to develop GMFs for Aquarius, which relate the microwave backscatter or excess surface emissivity to the wind speed (w) and direction (ϕ), which is the wind direction relative to the radar look angle. We use the following cosine series for the modeling of radar data:

$$\sigma_{VV}(w, \phi) = A_{0VV}(w) [1 + A_{1VV}(w) \cos \phi + A_{2VV}(w) \cos 2\phi] \quad (8)$$

$$\sigma_{HH}(w, \phi) = A_{0HH}(w) [1 + A_{1HH}(w) \cos \phi + A_{2HH}(w) \cos 2\phi]. \quad (9)$$

Here, σ_{VV} and σ_{HH} are the normalized radar backscatter cross section for V-transmit/V-receive and H-transmit/H-receive, respectively, and the A coefficients are estimated independently for each of Aquarius' antenna beams (incidence angles).

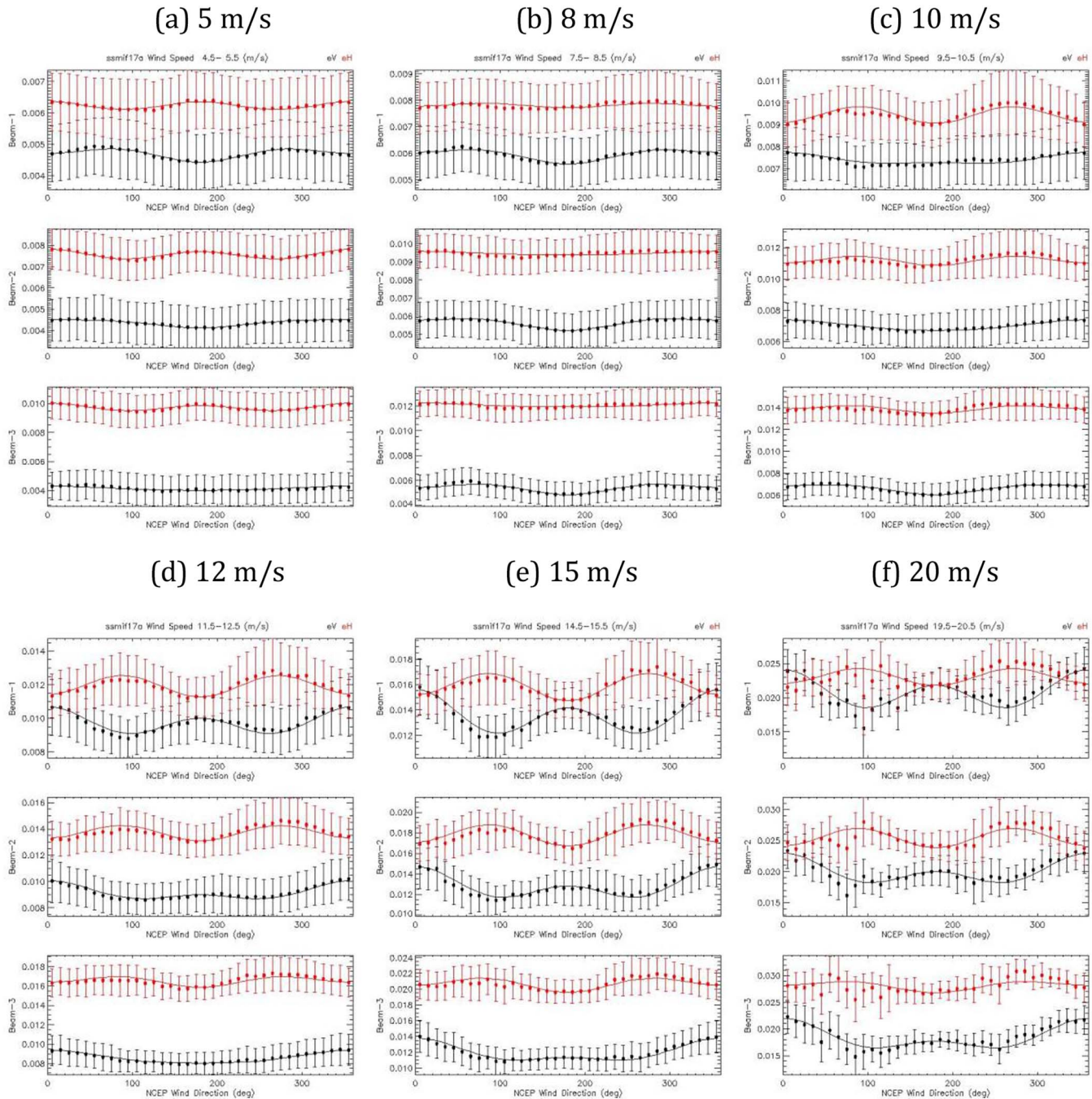


Fig. 2. Aquarius excess surface emissivity versus NCEP wind direction for six SSM/I wind speeds. In each wind speed panel, the upper row is for beam 1, the middle row is for beam 2, and the bottom row is for beam 3. Black and red dots are the binned matchup averages; vertical bars indicate ± 1 SD. Black and red curves are the three-term cosine series fit for T_{BV} and T_{BH} , respectively. (a) 5 m/s. (b) 8 m/s. (c) 10 m/s. (d) 12 m/s. (e) 15 m/s. (f) 20 m/s.

The modeling (A_0) coefficients for VV and HH are illustrated as a function of the SSM/I or NCEP wind speed in the upper row of Fig. 4. The HH A_0 agrees very well with PALSAR's GMF for all antenna beams for up to $15\text{ m}\cdot\text{s}^{-1}$ wind speeds. Above that, Aquarius' GMF should be more accurate because the PALSAR GMF was constructed with fewer matchups with the ASCAT winds above 15 m/s. The results from the SSM/I and NCEP matchups are very similar. Note that the natural values of A_0 are shown, not the decibel values. In general, A_0 increases with wind speed but seems to have a relatively smaller increase in the range of $4\text{--}8\text{ m}\cdot\text{s}^{-1}$. In particular, A_0 for beam

3 VV has almost no response to wind speed in this range of wind speeds but seems to exhibit an increasing trend above $10\text{ m}\cdot\text{s}^{-1}$.

The A_1 coefficients in the middle row of Fig. 4 increase with wind speed. The black and red solid curves in the panels are the piecewise linear interpolation of the data points. The agreement with the PALSAR A_1 is very good, although the Aquarius data do indicate deviations from the linear increase. It is noted that A_1 for VV is smaller by about a factor of two than that for HH. Comparing the A_1 between antenna beams (middle-row left to middle-row right panels) suggests an increase in A_1

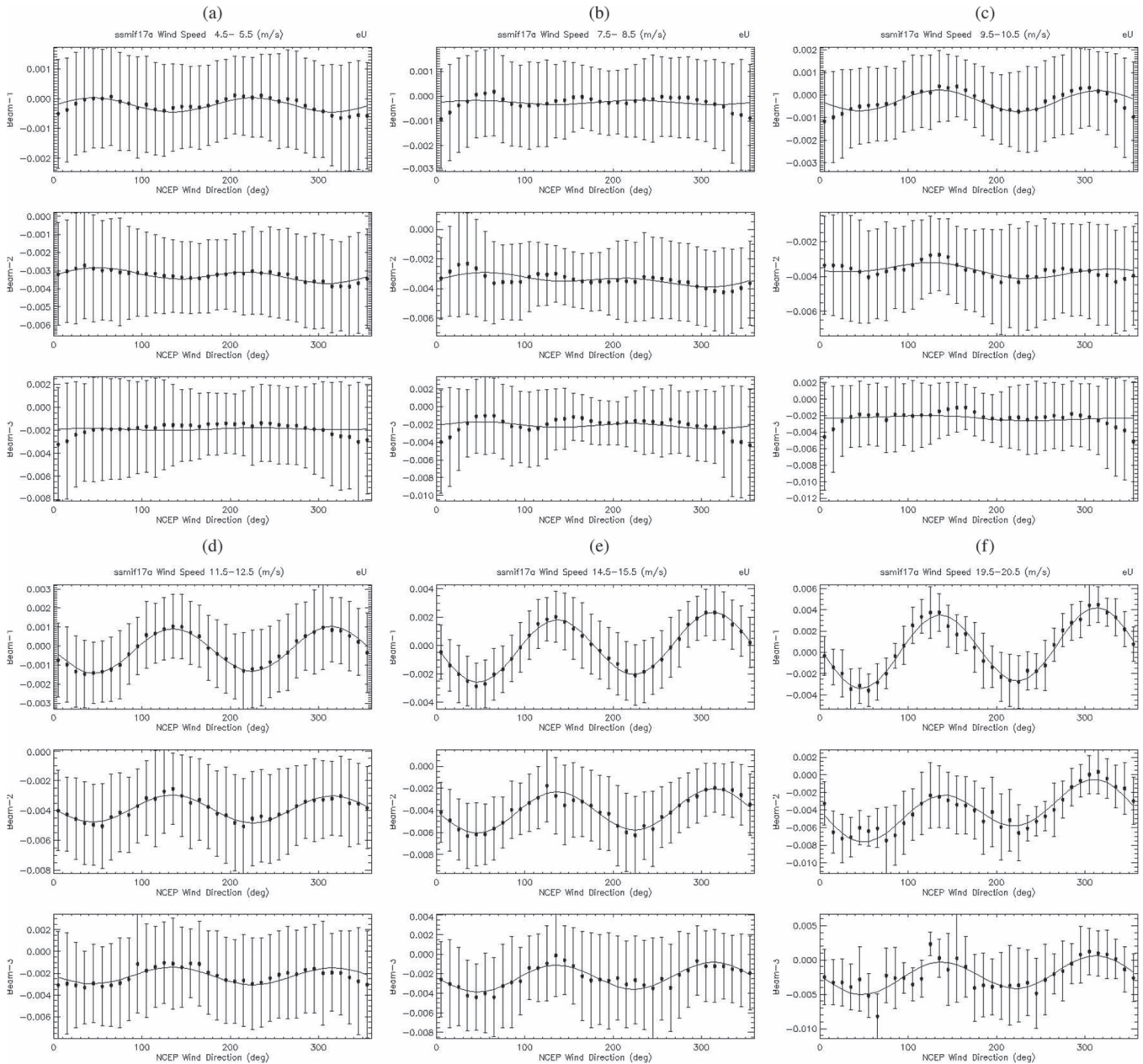


Fig. 3. Aquarius excess surface emissivity for the third Stokes (U) versus NCEP wind direction for six SSM/I wind speeds. In each wind speed panel, the upper row is for beam 1, the middle row is for beam 2, and the bottom row is for beam 3. Dots are data, vertical bars indicate ± 1 SD, and black curves are the sinusoidal fits. (a) 5 m/s. (b) 8 m/s. (c) 10 m/s. (d) 12 m/s. (e) 15 m/s. (f) 20 m/s.

versus incidence angle. The characteristics of polarization and incidence angle dependence are consistent with those at C- and Ku-band frequencies.

The characteristics of A_2 are illustrated in the bottom row of Fig. 4. There is not much difference between VV and HH, suggesting that the UC differences are essentially driven by the same scattering mechanisms for both polarizations. As we have discussed earlier, the A_2 coefficients have a phase transition from negative to positive at about $8\text{ m} \cdot \text{s}^{-1}$ wind speed. Overall, Aquarius' A_2 for HH agrees reasonably well with PALSAR's, particularly for beam 2, while the difference from PALSAR is larger for beam 3, although the shapes of the curves for A_2 versus wind speed are similar for beams 2 and 3. The difference for wind speeds lower than $5\text{ m} \cdot \text{s}^{-1}$ is likely caused by the use of different wind product for matchup:

PALSAR analysis used the ASCAT wind for matchup [4], while our Aquarius analysis used SSM/I or NCEP. The Aquarius data acquired at very low wind speeds suggest that there is a positive to negative transition at about $3\text{ m} \cdot \text{s}^{-1}$. The NUC scattering mechanism causing the negative A_2 between 3 and $8\text{ m} \cdot \text{s}^{-1}$ is unknown at this time.

The decrease of the directional harmonics (A_1 and A_2) for very high winds was suggested by higher frequency microwave measurements and PALSAR's A_2 coefficients (blue curves at the bottom panel of Fig. 4), which all suggested that the ocean surfaces and waves will become less and less directional above a certain threshold wind speed, which is about $20\text{ m} \cdot \text{s}^{-1}$. It is likely that breaking waves and sea foam are the key sources of reduction in directionality. Their scattering signatures are expected to be more isotropic than wind-generated

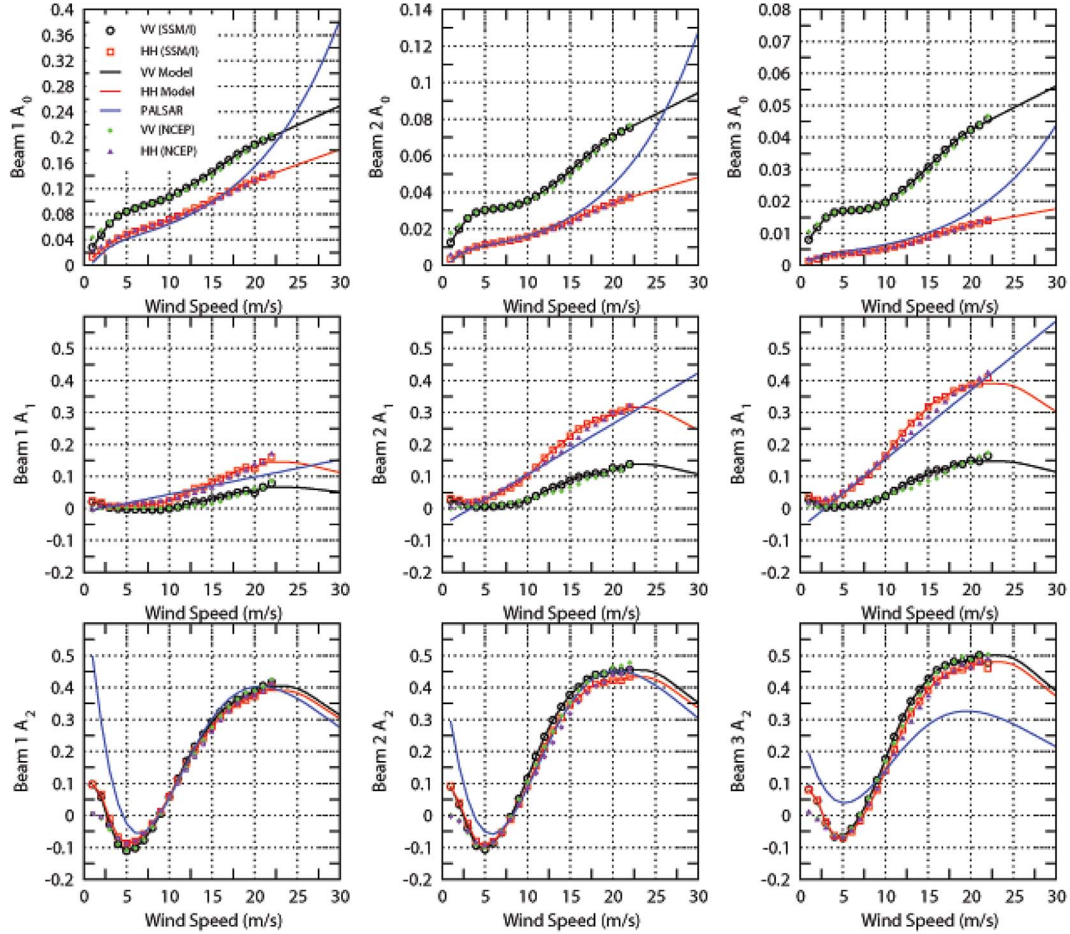


Fig. 4. Aquarius radar modeling coefficients (A_n) versus wind speed. The left column is for beam 1, the middle column is for beam 2, and the right column is for beam 3. Black circles and red squares are for the VV and HH matchups with the SSM/I wind speed, respectively. Green diamonds and orange triangles are for the matchups with the NCEP wind speed. The solid black and red curves are the piecewise linear interpolations of the matchups with the SSM/I wind speed. The blue curves correspond to the PALSAR HH GMF.

waves. Therefore, as their spatial coverage increases with wind speed, the total backscatter from sea surfaces will become less directional.

For the radiometer model function, we use the following expressions to characterize the dependence of excess surface emissivity on wind speed and direction:

$$\Delta e_V(w, \phi) = e_{V0}(w) + e_{V1}(w) \cos \phi + e_{V2}(w) \cos 2\phi \quad (10)$$

$$\Delta e_H(w, \phi) = e_{H0}(w) + e_{H1}(w) \cos \phi + e_{H2}(w) \cos 2\phi \quad (11)$$

$$u(w, \phi) = u_1(w) \sin \phi + u_2(w) \sin 2\phi. \quad (12)$$

The third Stokes parameter for the L-band frequency is modeled by the sine function of the wind direction, like the higher frequency observations [14]–[17]. The e and u coefficients are estimated for each beam independently.

The isotropic components (e_{V0} and e_{H0}) of the excess surface emissivity are illustrated at the top row of Fig. 5. As shown, the horizontal polarization is slightly more sensitive to the wind speed than the vertical polarization for beam 1 and about a factor of two more sensitive for beam 3. There is a monotonic increase in these components with incidence angle. However, similar to the behavior of scatterometer A_{0VV} , the slope of e_{V0} and e_{H0} appears to level off slightly between 5

and $10 \text{ m} \cdot \text{s}^{-1}$. Above $10 \text{ m} \cdot \text{s}^{-1}$, the increase is approximately linear with wind speed.

Fig. 5 includes results for both sets of matchups using either SSM/I wind speed or NCEP wind speed for binning. The differences between these two sets of matchups are mostly small. The only difference worthy of discussion is the e_{H0} for horizontal polarization at very low wind speeds ($< 3 \text{ m} \cdot \text{s}^{-1}$). The e_{H0} for the SSM/I matchup approaches very close to zero when the wind speed reduces to zero. However, e_{H0} for the NCEP matchup seems to have a fairly large residual value, about 0.002–0.003, at $0 \text{ m} \cdot \text{s}^{-1}$. This is probably an indication of a smaller random error in the SSM/I wind speed than in the NCEP or a better representation of the SSM/I wind for the surface roughness for light winds. For the $0\text{--}0.5 \text{ m} \cdot \text{s}^{-1}$ bin, the wind speed is in the range of $0\text{--}0.5 \text{ m} \cdot \text{s}^{-1}$. For a given NCEP wind speed in the $0\text{--}0.5 \text{ m} \cdot \text{s}^{-1}$ bin, the true wind speed may be much larger, or there could be the presence of swell, which prevents the surface from being completely smooth even at zero wind speed, leading to a smearing of the e_{H0} values in the lowest few wind speed bins. In contrast, the SSM/I wind speed for light winds is essentially a reflection of surface roughness; thus, the Aquarius excess surface emissivity will have a better correlation with SSM/I's wind speed (or roughness measure).

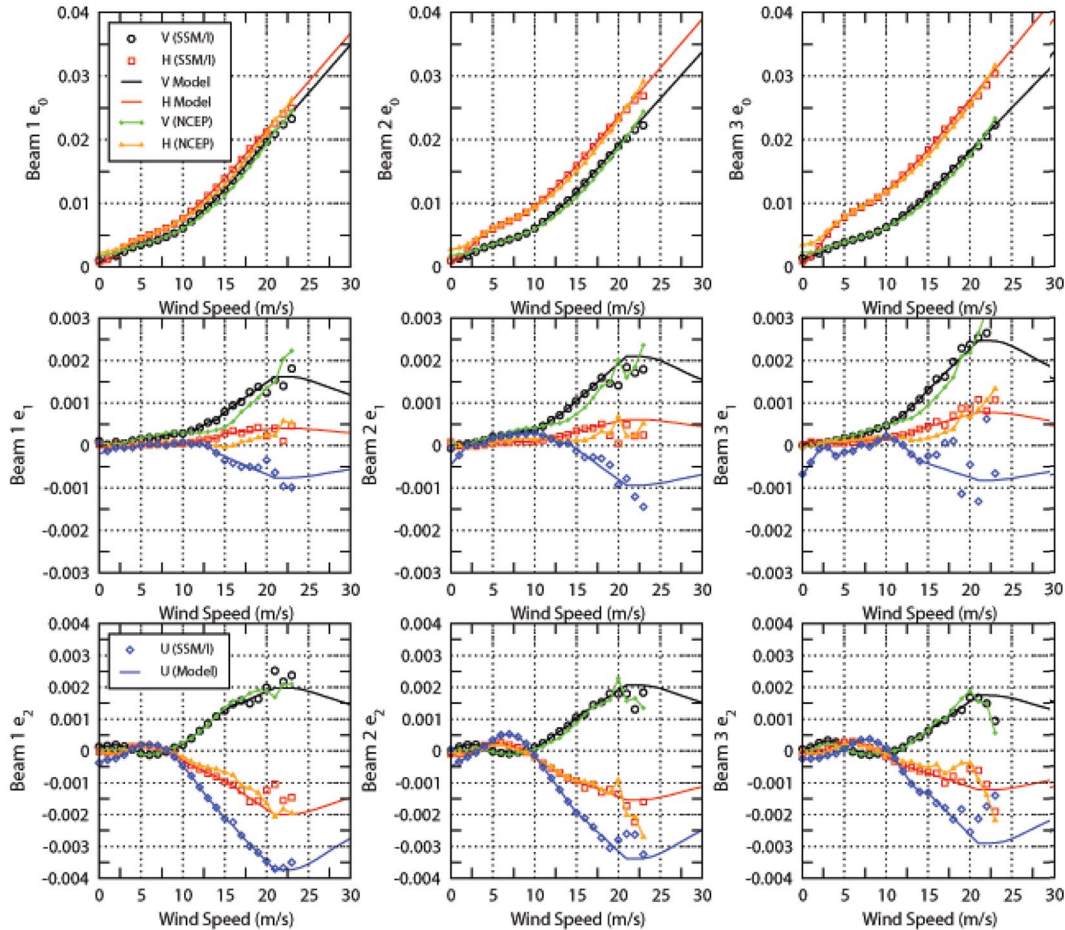


Fig. 5. Aquarius modeling coefficients (e_n and u_n) for excess surface emissivity versus wind speed. The left column is for beam 1, the middle column is for beam 2, and the right column is for beam 3. Black circles and red squares are for the V and H matchups with the SSM/I wind speed, respectively. Green diamonds and orange triangles are for the matchups with the NCEP wind speed. The solid black and red curves are the piecewise linear interpolations of the matchups with the SSM/I wind speed. Blue curves and diamonds represent the model and data for u_1 and u_2 .

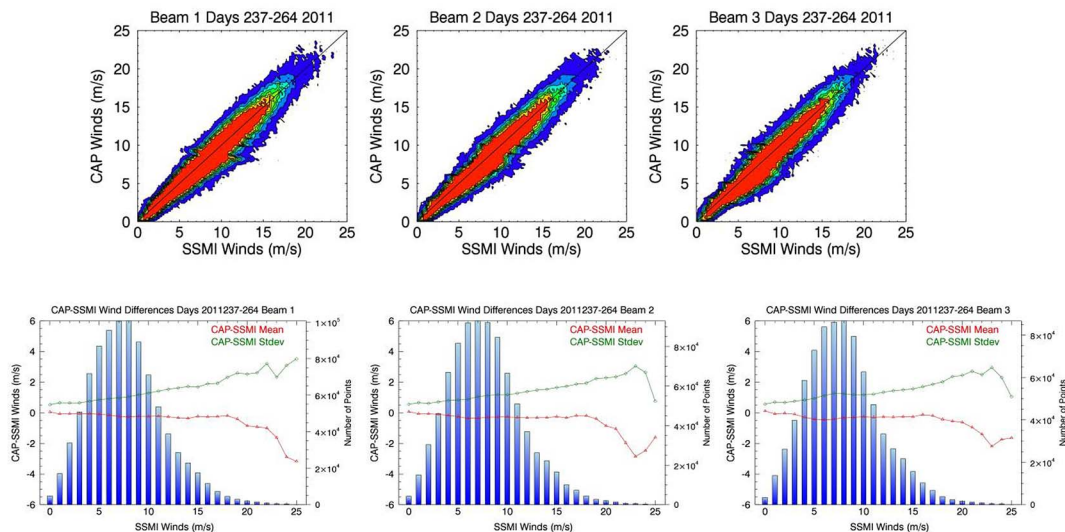


Fig. 6. Wind speed retrievals from the CAP algorithm are compared with the SSM/I wind speed. The scatter and statistics are illustrated for the first 28 days of data, but the results are essentially the same for other periods. The upper row illustrates the scatter with respect to the SSM/I wind speeds for (left) beam 1, (middle) beam 2, and (right) beam 3. The bottom row shows the bias and SD of the differences from the SSM/I wind speeds. The bar plots in the background are the wind speed histograms.

The amplitude of the first harmonic coefficients (e_{V1} , e_{H1} , and u_1), characterizing the upwind-downwind asymmetry of the excess surface emissivity, increases with increasing wind

speed (the middle row of Fig. 5). The NCEP matchups produce very similar results. The relative polarization behavior is consistent with the characteristics of high-frequency observations

at X-, K-, and Ka-band [14]–[16]: There is larger first harmonic amplitude for vertical polarization than for horizontal polarization.

The second harmonic coefficients (e_{V2} , e_{H2} , and u_2) are generally quite small for wind speeds less than $10 \text{ m} \cdot \text{s}^{-1}$ (bottom row of Fig. 5). Above $10 \text{ m} \cdot \text{s}^{-1}$, e_{V2} appears to increase linearly until the wind speed reaches $20 \text{ m} \cdot \text{s}^{-1}$, while e_{H2} appears to vary in opposite phase to e_{V2} . The amplitudes are about the same for V and H polarizations for beam 1, which operates at about 29° incidence angle, while the polarization asymmetry becomes more apparent for beam 3, operating at an incidence angle of about 46° . It appears that the phase transitions of e_{V2} , e_{H2} , and u_2 at about 3 and $8 \text{ m} \cdot \text{s}^{-1}$ corroborate that of the scatterometer A_2 at the same wind speeds. The consistent signatures of phase transition of the UC asymmetry in both the passive and active microwave support the existence of the NUC scattering mechanism for sea surfaces at L-band.

Given the GMF for excess surface emissivity, the following are the complete descriptions of the radiometer model function, which relates the brightness temperatures to SSS, SST, and wind speed and direction

$$T_{BV}(\text{SSS}, \text{SST}, w, \phi) = T_{BV\text{flat}}(\text{SSS}, \text{SST}) + \text{SST} \cdot \Delta e_V(w, \phi) \quad (13)$$

$$T_{BH}(\text{SSS}, \text{SST}, w, \phi) = T_{BH\text{flat}}(\text{SSS}, \text{SST}) + \text{SST} \cdot \Delta e_H(w, \phi) \quad (14)$$

$$U(\text{SST}, w, \phi) = \text{SST} \cdot u(w, \phi). \quad (15)$$

The aforementioned model functions are evaluated for each Aquarius antenna beam or incidence angle. The current form of GMFs includes a set of text tables with the model coefficients (e_n and A_n) tabulated at $1\text{-m} \cdot \text{s}^{-1}$ step size together with linear interpolation between wind speed steps. We have examined the polynomial fitting of the modeling coefficients versus wind speed and have found that a fifth-order polynomial fit can provide a very good representation from 0- to 25-m/s wind speed. However, when applied to the retrievals (Section IV), the polynomial fit does not provide as accurate results as the tabular format with linear interpolation.

IV. MODEL FUNCTION TESTING THROUGH WIND AND SSS RETRIEVAL

The GMFs derived from the Aquarius and SSM/I or NCEP matchup data sets represent the mean microwave backscatter or emission from the ocean surface within a given wind speed/direction bin. However, the sea surface roughness can be influenced by several parameters, such as significant wave height or boundary layer stability, other than the winds. The matchup analyses have not provided the uncertainty of the GMFs in terms of the impact of many other parameters on sea surface roughness.

The uncertainty of the GMFs for excess surface emissivity and radar backscatter is assessed by applying them to the Aquarius data for wind and salinity retrieval. By examining the accuracy of wind retrievals through comparison with the SSM/I and NCEP winds, we will close the loop to independently confirm the accuracy of the GMFs.

A. Overview of CAP Algorithm

The current approach of the Aquarius salinity retrieval algorithm requires the use of ancillary NCEP surface wind direction to make corrections to ocean brightness temperatures. Any errors in the NCEP analyses, particularly for high winds or near a front, as well as temporal mismatch with the Aquarius sampling, may not allow the directional effects to be accurately removed. To remove the dependence on the NCEP wind direction for retrieval, the combined active–passive (CAP) algorithm was developed to retrieve the salinity and wind without the need to use the NCEP winds for corrections [33].

The CAP algorithm simultaneously retrieves the salinity and wind speed and direction by minimizing the sum of squared differences between model and observations. After testing the CAP algorithm against the Aquarius data, we find that the following expression for least square error (LSE) performs very well:

$$F_{\text{cap}}(\text{SSS}, w, \phi) = \frac{(I - I_m)^2}{2\Delta T^2} + \frac{(\sqrt{Q^2 + U^2} - \sqrt{Q_m^2 + U_m^2})^2}{2\Delta T^2} + \frac{(\sigma_{VV} - \sigma_{VVm})^2}{k_{\text{pc}}^2 \sigma_{VV}^2} + \frac{(\sigma_{HH} - \sigma_{HHm})^2}{k_{\text{pc}}^2 \sigma_{HH}^2}. \quad (16)$$

In the aforementioned equation, I , Q , U , σ_{VV} , and σ_{HH} represent measurements, while the quantities with the subscript “m” correspond to the model functions described by (8), (9), (12), –(15). The difference between data and model is weighted by the expected uncertainty of measurements. For radiometer data, the minimum uncertainty is the NEDT (ΔT). The precision of radar data is limited by the expected signal detection error (k_{pc}). For Aquarius, ΔT is about 0.1 K, and k_{pc} is about 0.01.

The first Stokes parameter ($I = T_{BV} + T_{BH}$) represents the total power of the microwave emission and is not changed by any polarization rotation. The second Stokes parameter (Q) is influenced by Faraday rotation, just like the third Stokes parameter (U), but the sum of the squares of Q and U is another invariant quantity under Faraday rotation

$$I_{QU} = \sqrt{Q^2 + U^2}. \quad (17)$$

The invariance of I_{QU} under Faraday rotation can be easily shown by using (3) and (4).

Because I and I_{QU} are invariant under Faraday rotation or any other polarization rotations due to instrument misalignment or spacecraft attitude changes, we can use the surface brightness temperatures T_{BV} and T_{BH} in the Aquarius L2 files for the computation of I and I_{QU} terms in F_{cap} (16). Although T_{BV} and T_{BH} in the Aquarius files are influenced by the inaccurate (or imperfect) assumption of $U = 0$ for Faraday rotation correction, I and I_{QU} derived from them are not. The use of I and I_{QU} , rather than T_{BV} and T_{BH} , makes the CAP F_{cap} formulation insensitive to the bright temperature errors resulting from inaccurate Faraday rotation corrections.

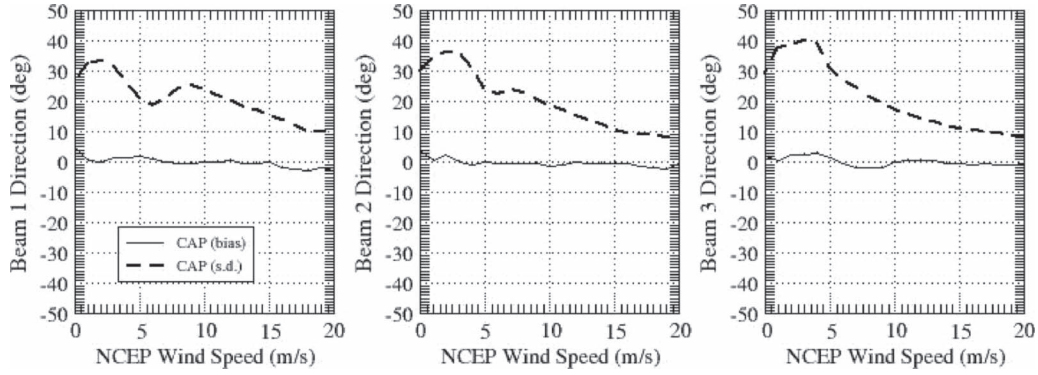


Fig. 7. Wind direction retrievals from the CAP algorithm are compared with the NCEP wind direction for the first four weeks of 2012. The results for other time periods are similar. The left (beam 1), middle (beam 2), and right (beam 3) plots show the bias and SD of the differences from the NCEP wind direction.

For radar σ_{VV} and σ_{HH} measurements, the impact of Faraday rotation is fairly small, less than 0.1 dB for a Faraday rotation angle of 5° . However, we have applied the Faraday rotation angle estimated from the IGS-IONEX TEC product to make corrections. The residual errors are a few times smaller and are therefore negligible.

For the Aquarius data, we applied the conjugate gradient technique using a modified Levenberg–Marquardt algorithm [34] to find the local minima of the LSE. There are, in general, four local minima (ambiguous solutions). This is due to the expansion of the model function for wind direction by including up to the second harmonics of the cosine series. For each given wind speed solution, there will, in general, be four direction solutions, except when the relative wind direction is along upwind, downwind, or crosswind. This can be easily understood by considering the special case when the A_1 coefficients are zero in the model functions. If the first harmonic coefficient A_1 is zero, these four solutions, corresponding to the inversion of $\cos 2\phi$, are ϕ , $-\phi$, $\phi + 180^\circ$, and $180^\circ - \phi$. If A_1 and e_1 are small, then the third and fourth solutions will shift slightly away from $\pm\phi + 180^\circ$. Because the cosine series are even functions, the solution pair $\pm\phi$ will produce identical values for model functions and will consequently lead to the same SSS and wind speed solutions. The same is true for the $\pm\phi + 180^\circ$ solution pair.

A nominal ambiguity removal technique developed for the current or past spaceborne wind scatterometer and radiometer missions is the use of numerical weather analysis, such as NCEP ECMWF, or special wind features to assist in the selection [25]. For salinity and wind speed retrievals, the discrimination of ambiguities is a less challenging issue than that for ocean wind scatterometers or radiometers because what is needed is to separate the four solutions into two pairs, namely, $\pm\phi$ and $\pm\phi + 180^\circ$, which are separated by about 180° . As previously discussed, each pair will have the same SSS and wind speed values. In our analysis, we use the numerical wind analyses to select the solution with the wind direction closest to NCEP.

B. Results of Speed and Direction Retrievals

Fig. 6 illustrates the scatter of the retrieved wind speed with respect to the SSM/I wind speed in the upper row. The scatter is reasonably tight along the ideal diagonal line for

each antenna beam. The lower panels indicate the mean and standard deviation (SD) of differences binned as a function of the SSM/I wind speed. The mean difference (bias) is close to zero, which means that the retrieval is essentially unbiased with respect to the SSM/I wind speed. The negative bias at very high wind speed above $23 \text{ m} \cdot \text{s}^{-1}$ is most likely an artifact of the matchup error analysis; the estimated bias can be expected to be negative by comparing a noisy wind speed estimate with a noisy wind reference (SSM/I) according to [35]. It is shown that the SD of the differences is quite small, reaching as low as $0.5 \text{ m} \cdot \text{s}^{-1}$ for very low winds, and remains less than $2 \text{ m} \cdot \text{s}^{-1}$ up to $15 \text{ m} \cdot \text{s}^{-1}$.

Fig. 7 indicates the differences between retrieved wind directions and NCEP's. The mean differences are near zero across the entire range of wind speed or essentially unbiased. The SDs, in general, are quite large, greater than 20° for less than $8 \text{ m} \cdot \text{s}^{-1}$ wind speeds, where the directional signals in radar σ_0 and radiometer T_B are small. The SDs have a small dip for beam 1 near $5 \text{ m} \cdot \text{s}^{-1}$, at which A_2 has a local minimum with negative values, but deviate from zero near 3- or $8 \text{ m} \cdot \text{s}^{-1}$ wind speeds. The SDs reduce with increasing wind speed (or A_2 and e_2). The SDs for beam 2 and 3 are less than 20° above $9 \text{ m} \cdot \text{s}^{-1}$ wind speeds, while beam 1's SDs decrease to below 20° at about $12 \text{ m} \cdot \text{s}^{-1}$. The agreement with the NCEP wind direction justifies the parameterization of directional characteristics in the GMFs.

C. Triple Collocation Analysis

It is not possible to assess the accuracy of two noisy wind products by intercomparing them. The methodology of triple collocation analysis [35], [36] is the only known method to estimate the random errors and relative calibration factors of three independent products.

Without loss of generality, we use the SSM/I wind speed as the reference data set. For the triple collocation analysis, we assume the following error models for the three wind speed data sets, namely, SSM/I, NCEP, and Aquarius retrieval:

$$W_{\text{SSM/I}} = W + r_{\text{SSM/I}}$$

$$W_{\text{NCEP}} = A_{\text{NCEP}}W + B_{\text{NCEP}} + r_{\text{NCEP}}$$

$$W_{\text{AQ}} = A_{\text{AQ}}W + B_{\text{AQ}} + r_{\text{AQ}}.$$

TABLE I
RELATIVE SYSTEMATIC ERROR IN THE WIND SPEED
PRODUCTS FOR THE DATA ACQUIRED IN 2011

	SSM/I	NCEP	AQ-CAP
Beam 1 Slope A	1	1.020	1.043
Beam 2 Slope A	1	1.021	1.042
Beam 3 Slope A	1	1.032	1.052
Beam 1 bias B ($\text{m}\cdot\text{s}^{-1}$)	0	-0.19	-0.31
Beam 2 bias B ($\text{m}\cdot\text{s}^{-1}$)	0	-0.19	-0.33
Beam 3 bias B ($\text{m}\cdot\text{s}^{-1}$)	0	-0.27	-0.43

TABLE II
RANDOM ERRORS IN THE WIND SPEED PRODUCTS
FOR THE DATA ACQUIRED IN 2011

	SSM/I	NCEP	AQ-CAP
Beam 1 Random Error ($\text{m}\cdot\text{s}^{-1}$)	0.77	1.08	0.77
Beam 2 Random Error ($\text{m}\cdot\text{s}^{-1}$)	0.75	1.07	0.73
Beam 3 Random Error ($\text{m}\cdot\text{s}^{-1}$)	0.80	1.03	0.78

In the aforementioned equations, W is the true wind speed, A and B are the relative calibration (scale and bias) factors, and r is the random error. To enable the application of triple collocation to determine A , B , and r for each, the following assumptions are made.

- 1) SSM/I has no bias and no scale offset from true winds.
- 2) $\langle r_{\text{SSM/I}} r_{\text{NCEP}} \rangle = \langle r_{\text{SSM/I}} r_{\text{AQ}} \rangle = \langle r_{\text{NCEP}} r_{\text{AQ}} \rangle = 0$ (all errors uncorrelated).
- 3) $\langle r_{\text{SSM/I}} W \rangle = \langle r_{\text{NCEP}} W \rangle = \langle r_{\text{AQ}} W \rangle = 0$ (errors not correlated with true winds).

The results of the triple collocation analysis applied to the data collected in 2011 are summarized in Tables I and II. The relative calibration factor (A) for NCEP and AQ-CAP is very close to unity, within 2% and 5%, respectively. The relative scaling between NCEP and AQ-CAP will be about 2%. The calibration bias is also quite small, about $0.2\text{--}0.3 \text{ m}\cdot\text{s}^{-1}$ for NCEP and between 0.3 and $0.4 \text{ m}\cdot\text{s}^{-1}$ for Aquarius. Based on the same argument made in [35], it is likely that the systematic errors, relative calibration scaling and bias, are caused by the binning of two noisy data sets for the development of GMFs: Aquarius microwave data and SSM/I wind speed. The errors in the SSM/I wind speed and NCEP wind direction will cause the Aquarius microwave data to fall into the wrong bin, thus leading the GMFs to have a smoother response to the wind speed, which will cause the retrievals to have a scaling and bias error. However, the systematic errors, which can be tuned out by applying scaling adjustments to the GMFs, have very small influence on the estimate of random errors.

The AQ-CAP wind speed errors (r_{AQ}) in Table II are very small, about $0.75 \text{ m}\cdot\text{s}^{-1}$, better than the NCEP random error by about 30%–40%. The random errors for AQ-CAP and SSM/I are very close to each other, essentially within the uncertainty of the triple collocation analysis. We have also performed triple collocation analysis by using the NCEP as the reference (without bias and with slope equal to unity), and the resulting random errors are essentially unchanged.

From the random errors in wind speed, we can estimate the resulting random errors for brightness temperature corrections. For vertical polarization, the excess surface emissivity (e_{v0}) changes by about 0.006 from 0 to $10 \text{ m}\cdot\text{s}^{-1}$ (top row of Fig. 5).

The sensitivity of vertically polarized brightness temperatures to wind speed (dT_{BV}/dW) will be about $0.18 \text{ K}\cdot\text{m}\cdot\text{s}^{-1}$ in wind speed. Considering the random error indicated in Table II, we can estimate the parameterization error of the vertically polarized brightness temperature GMF by multiplying the random wind speed error (about $0.75 \text{ m}\cdot\text{s}^{-1}$) by the T_{B} sensitivity to wind (dT_{BV}/dW). The resulting estimates are 0.14 K, close to the desired accuracy for Aquarius.

The estimated residual T_{B} correction errors are consistent with the accuracy of salinity retrievals (Fig. 8). The SDs of the differences between AQ-CAP and HYCOM SSS are about 0.5 psu for wind speeds from 0 to $10 \text{ m}\cdot\text{s}^{-1}$ for all antenna beams. Because the global average change of T_{BV} for an SSS change of 1 psu is about 0.5 K, the corresponding T_{BV} residual error for 0.5 psu will be about 0.25 K. Note that Aquarius SSS errors include the effects of many error sources, in addition to surface roughness. The 0.25 K estimate should be an upper bound for the modeling error in the GMF, and it is consistent with the 0.14 K estimate obtained from wind speed error analyses.

V. SUMMARY

We have derived the L-band radar and radiometer model functions for ocean surface winds from Aquarius data. The GMFs show appreciable wind direction dependence at greater than $10 \text{ m}\cdot\text{s}^{-1}$ for all radar and radiometer polarizations. The agreement with the PALSAR HH model function and previous airborne data sets is excellent, and we have observed similar wind direction dependence in the VV polarization. The directional modulation in the radiometer T_{B} is highly significant for Aquarius' salinity retrieval and may result in a few practical salinity unit salinity retrieval error at high winds ($> 10 \text{ m}\cdot\text{s}^{-1}$).

We have found that the second harmonic coefficients (or the UC asymmetry) have a phase transition at about 3- and $8\text{--} \text{m}\cdot\text{s}^{-1}$ wind speeds for all Aquarius antenna beams, operating in the range of $29^\circ\text{--}46^\circ$ incidence angles. The responsible NUC scattering mechanism is unknown at this time. The nominal Bragg scattering mechanism in the two-scale models has not yet been able to produce the observed signatures. The Aquarius data set indicates the existence of some ocean surface features, which have not yet been investigated for microwave scattering modeling at L-band.

We have provided experimental evidence in the Aquarius data that there are wind direction signals, in the form of sine function of wind direction, in the third Stokes parameter of ocean emissions. The amplitude is small, only about 1–2 K peak to peak at about $15\text{--}20\text{--} \text{m}\cdot\text{s}^{-1}$ wind speeds. The magnitude does not have very much impact on the assumption of $U = 0$ for Faraday rotation correction of the Aquarius radiometer data but should still be considered to remove any systematic bias.

We have confirmed the validity of the GMFs by applying them to the Aquarius retrieval using the CAP algorithm for simultaneous wind and salinity retrieval. The retrieved wind speed has very good agreement with the SSM/I and NCEP wind products. The directional accuracy also appears to be very good above $10\text{--} \text{m}\cdot\text{s}^{-1}$ wind speeds. The triple collocation analysis suggests that the Aquarius CAP wind speed is highly accurate,

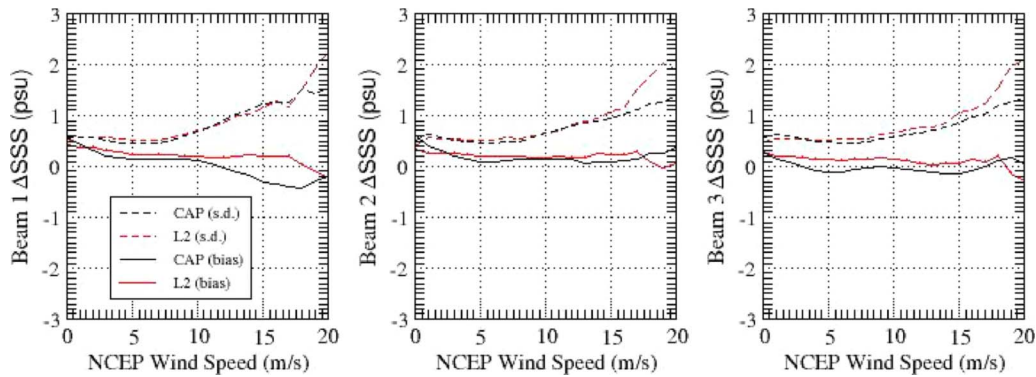


Fig. 8. SSS retrievals from the CAP algorithm are compared with the HYCOM salinity for the first four weeks of 2012. The left (beam 1), middle (beam 2), and right (beam 3) plots show the bias and SD of the differences from the HYCOM SSS. The black solid and dashed curves are for the CAP algorithm, while the red curves are for the Aquarius V1.3 retrievals.

about $0.75 \text{ m} \cdot \text{s}^{-1}$ in random errors, comparable to SSM/T's. The equivalent GMF modeling error is about 0.14 K for vertical polarization, close to the desired accuracy for Aquarius.

Note that it is important to recognize that we have neglected to consider the influence of several potential contributors to the modeling of microwave brightness temperatures and backscatter. For example, the ocean wave height and wave slope are known experimentally or theoretically to impact the ocean surface scattering and emission [9], [37]. In the future, impact analyses of these parameters will be considered to reduce the modeling error of surface roughness in the GMFs.

ACKNOWLEDGMENT

The work described in this paper was carried out by the Jet Propulsion Laboratory, California Institute of Technology, under a contract with the National Aeronautics and Space Administration.

REFERENCES

- [1] J. Font, A. Camps, A. Borges, M. Martin-Neira, J. Boutin, N. Reul, Y. H. Kerr, A. Hahne, and S. Mecklenburg, "SMOS: The challenging sea surface salinity measurement from space," *Proc. IEEE*, vol. 98, no. 5, pp. 649–665, May 2010.
- [2] G. Lagerloef, F. R. Colomb, D. Le Vine, F. Wentz, S. Yueh, C. Ruf, J. Lilly, J. Gunn, Y. Chao, A. deCharon, G. Feldman, and C. Swift, "The Aquarius/SAC-D mission: Designed to meet the salinity remote-sensing challenge," *Oceanography*, vol. 21, no. 1, pp. 68–81, Mar. 2008.
- [3] D. Entekhabi, E. G. Njoku, P. E. O'Neill, K. H. Kellogg, W. T. Crow, W. N. Edelstein, J. K. Entin, S. D. Goodman, T. J. Jackson, J. Johnson, J. Kimball, J. R. Piepmeier, R. D. Koster, N. Martin, K. C. McDonald, M. Moghaddam, S. Moran, R. Reichle, J. C. Shi, M. W. Spencer, S. W. Thurman, L. Tsang, and J. Van Zyl, "The Soil Moisture Active Passive (SMAP) mission," *Proc. IEEE*, vol. 98, no. 5, pp. 704–716, May 2010.
- [4] O. Isoguchi and M. Shimada, "An L-band ocean geophysical model function derived from PALSAR," *IEEE Trans. Geosci. Remote Sens.*, vol. 47, no. 7, pp. 1925–1936, Jul. 2009.
- [5] S. H. Yueh, R. West, W. J. Wilson, F. K. Li, E. G. Njoku, and Y. Rahmat-Samii, "Error sources and feasibility for microwave remote sensing of ocean surface salinity," *IEEE Trans. Geosci. Remote Sens.*, vol. 39, no. 5, pp. 1049–1060, May 2001.
- [6] J. P. Hollinger, "Passive microwave measurements of sea surface roughness," *IEEE Trans. Geosci. Electron.*, vol. GE-9, no. 3, pp. 165–169, Jul. 1971.
- [7] A. Camps, J. Font, M. Vall-Llossera, C. Gabarro, I. Corbella, N. Duffo, F. Torres, S. Blanch, A. Aguasca, R. Villarino, L. Enrique, J. J. Miranda, J. J. Arenas, A. Juliaa, J. Etcheto, V. Caselles, A. Weill, J. Boutin, S. Contardo, R. Niclos, R. Rivas, S. C. Reising, P. Wursteisen, M. Berger, and M. Martin-Neira, "The WISE 2000 and 2001 field experiments in support of the SMOS mission: Sea surface L-band brightness temperature observations and their application to sea surface salinity retrieval," *IEEE Trans. Geosci. Remote Sens.*, vol. 42, no. 4, pp. 804–823, Apr. 2004.
- [8] J. Etcheto, E. P. Dinnat, J. Boutin, A. Camps, J. Miller, Stephanie, J. Wesson, J. Font, and D. Long, "Wind speed effect on L-Band brightness temperature inferred from EuroSTARRS and WISE 2001 field experiments," *IEEE Trans. Geosci. Remote Sens.*, vol. 42, no. 10, pp. 2206–2213, Oct. 2004.
- [9] C. Gabarro, J. Font, A. Camps, M. Vall-Llossera, and A. Julia, "A new empirical model of sea surface microwave emissivity for salinity remote sensing," *Geophys. Res. Lett.*, vol. 31, no. 1, pp. L01309-1–L01309-5, Jan. 2004.
- [10] A. Camps, M. Vall-Llossera, R. Villarino, N. Reul, B. Chapron, I. Corbella, N. Duffo, F. Torres, J. J. Miranda, R. Sabia, A. Monerris, and R. Rodriguez, "The emissivity of foam-covered water surface at L-band: Theoretical modeling and experimental results from the FROG 2003 field experiment," *IEEE Trans. Geosci. Remote Sens.*, vol. 43, no. 5, pp. 925–937, May 2005.
- [11] S. H. Yueh, S. Dinardo, A. Fore, and F. Li, "Passive and active L-band microwave observations and modeling of ocean surface winds," *IEEE Trans. Geosci. Remote Sens.*, vol. 48, no. 8, pp. 3087–3100, Aug. 2010.
- [12] X. Yin, J. Boutin, N. Martin, and P. Spurgeon, "Optimization of L-band sea surface emissivity models deduced from SMOS data," *IEEE Trans. Geosci. Remote Sens.*, vol. 50, no. 5, pp. 1414–1426, May 2012.
- [13] N. Reul, J. Tenerelli, B. Chapron, D. Vandemark, Y. Quilfen, and Y. Kerr, "SMOS satellite L-band radiometer: A new capability for ocean surface remote sensing in hurricanes," *J. Geophys. Res.—Oceans*, vol. 117, no. C2, pp. C02006-1–C02006-24, Feb. 2, 2012.
- [14] S. H. Yueh, W. J. Wilson, S. Dinardo, and F. K. Li, "Polarimetric microwave brightness signatures of ocean wind directions," *IEEE Trans. Geosci. Remote Sens.*, vol. 37, no. 2, pp. 949–959, Mar. 1999.
- [15] J. R. Piepmeier and A. J. Gasiewski, "High-resolution passive polarimetric microwave mapping of ocean surface wind vector fields," *IEEE Trans. Geosci. Remote Sens.*, vol. 39, no. 3, pp. 606–622, Mar. 2001.
- [16] S. H. Yueh, W. Wilson, S. Dinardo, and S. V. Hsiao, "Polarimetric microwave wind radiometer model function and retrieval testing for WindSat," *IEEE Trans. Geosci. and Remote Sensing*, vol. 44, no. 3, pp. 584–596, Mar. 2006.
- [17] S. Yueh, "Directional signals in WindSat observations of hurricane ocean winds," *IEEE Trans. Geosci. Remote Sens.*, vol. 46, no. 1, pp. 130–136, Jan. 2008.
- [18] P. W. Gaiser, K. M. St. Germain, E. M. Twarog, G. A. Poe, W. Purdy, D. Richardson, W. Grossman, W. L. Jones, D. Spencer, G. Golba, J. Cleveland, L. Choy, R. M. Bevilacqua, and P. S. Chang, "The WindSat spaceborne polarimetric microwave radiometer: Sensor description and early orbit performance," *IEEE Trans. Geosci. Remote Sens.*, vol. 42, no. 11, pp. 2347–2361, Nov. 2004.
- [19] S. H. Yueh, "Estimates of Faraday rotation with passive microwave polarimetry for microwave remote sensing of Earth surfaces," *IEEE Trans. Geosci. Remote Sens.*, vol. 38, no. 5, pp. 2434–2438, Sep. 2000.
- [20] D. M. Le Vine, G. S. E. Lagerloef, R. Coloma, S. Yueh, and F. Pellerano, "Aquarius: An instrument to monitor sea surface salinity from space," *IEEE Trans. Geosci. Remote Sens.*, vol. 45, no. 7, pp. 2040–2050, Jul. 2007.

- [21] SSM/I Products Produced by the Remote Sensing System. [Online]. Available: http://www.ssmi.com/ssmi/ssmi_description.html
- [22] NCEP Global Forecast System Products. [Online]. Available: http://nomads.nccdc.noaa.gov/data.php#hires_weather_datasets
- [23] R. W. Reynolds, T. M. Smith, C. Liu, D. B. Chelton, K. S. Casey, and M. G. Schlax, "Daily high-resolution blended analyses for sea surface temperature," *J. Climate*, vol. 20, no. 22, pp. 5473–5496, Nov. 2007.
- [24] E. P. Chassignet, H. E. Hurlburt, E. J. Metzger, O. M. Smedstad, J. Cummings, G. R. Halliwell, R. Bleck, R. Baraille, A. J. Wallcraft, C. Lozano, H. L. Tolman, A. Srinivasan, S. Hankin, P. Cornillon, R. Weisberg, A. Barth, R. He, F. Werner, and J. Wilkin, "U.S. GODAE: Global ocean prediction with the HYbrid Coordinate Ocean Model (HYCOM)," *Oceanography*, vol. 22, no. 2, pp. 64–75, Jun. 2009.
- [25] M. W. Spencer, C. Wu, and D. G. Long, "Improved resolution backscatter measurements with the SeaWinds pencil-beam scatterometer," *IEEE Trans. Geosci. Remote Sens.*, vol. 38, no. 1, pp. 89–104, Jan. 2000.
- [26] J. Figa-Saldaña, J. J. W. Wilson, E. Attema, R. Gelsthorpe, M. R. Drinkwater, and A. Stoffelen, "The Advanced Scatterometer (ASCAT) on the Meteorological Operational (MetOp) platform: A follow on for European wind scatterometers," *Can. J. Remote Sens.*, vol. 28, no. 3, pp. 404–412, Jun. 2002.
- [27] S. T. Wu and A. K. Fung, "A noncoherent model for microwave emissions and backscattering from the sea surface," *J. Geophys. Res.*, vol. 77, no. 30, pp. 5917–5929, Oct. 1972.
- [28] V. N. Kudryavtsev, D. Hauser, G. Caudal, and B. Chapron, "A semiempirical model of the normalized radar cross-section of the sea surface, 1. Background model," *J. Geophys. Res.*, vol. 108, no. C3, pp. 8054–8078, Mar. 2003.
- [29] J. D. Kraus, *Radio Astronomy*, 2nd ed. Powell, OH, USA: Cygnus-Quasar Books, 1986.
- [30] International GNSS Service TEC Products. [Online]. Available: <http://igsweb.jpl.nasa.gov/components/prods.html>
- [31] C. C. Finlay, S. Maus, C. D. Beggan, T. N. Bondar, A. Chambodut, T. A. Chernova, A. Chulliat, V. P. Golovkov, B. Hamilton, M. Hamoudi, R. Holme, G. Hulot, W. Kuang, B. Langlais, V. Lesur, F. J. Lowes, H. Lühr, S. Macmillan, M. Manda, S. McLean, C. Manoj, M. Menvielle, I. Michaelis, N. Olsen, J. Rauberg, M. Rother, T. J. Sabaka, A. Tangborn, L. Tøffner-Clausen, E. Thébaud, A. W. P. Thomson, I. Wardinski, Z. Wei, and T. I. Zvereva, "International Geomagnetic Reference Field: The eleventh generation," *Geophys. J. Int.*, vol. 183, no. 3, pp. 1216–1230, Dec. 2010.
- [32] T. Meissner and F. Wentz, "The complex dielectric constant of pure and sea water from microwave satellite observations," *IEEE Trans. Geosci. Remote Sens.*, vol. 42, no. 9, pp. 1836–1849, Sep. 2004.
- [33] S. Yueh and J. Chaubell, "Sea surface salinity and wind retrieval using combined passive and active L-band microwave observations," *IEEE Trans. Geosci. Remote Sens.*, vol. 50, no. 4, pp. 1022–1032, Apr. 2012.
- [34] Burton, S. Garbow, K. E. Hillstrom, and J. J. More, "Documentation for Minpack," Argonne National Laboratory, Lemont, IL, USA.
- [35] A. Stoffelen, "Toward the true near-surface wind speed: Error modeling and calibration using triple collocation," *J. Geophys. Res.*, vol. 103, no. C4, pp. 7755–7766, Apr. 15, 1998.
- [36] J. Vogelzang, A. Stoffelen, A. Verhoef, and J. Figa-Saldaña, "On the quality of high-resolution scatterometer winds," *J. Geophys. Res.*, vol. 116, no. C10, pp. C10033–1–C10033–14, Oct. 2011.
- [37] Y. Quilfen, B. Chapron, F. Collard, and D. Vandemark, "2004: Relationship between ERS scatterometer measurement and integrated wind and wave parameters," *J. Atmos. Ocean. Technol.*, vol. 21, no. 2, pp. 368–373, Feb. 2004.

the Project Scientist of the National Aeronautics and Space Administration (NASA) Aquarius mission for global sea surface salinity observations from January 2012 to September 2013. He has been the Project Scientist of the NASA Soil Moisture Active–Passive Mission since October 2013. He has been the Principal/Coinvestigator of numerous research projects, including the polarimetric wind radiometer research, airborne scatterometer project for hurricane wind measurements, Passive/Active L-band Sensor (PALS) project, NASA Instrument Incubator Project for a mission concept using a large mesh-deployable antenna for soil moisture and ocean salinity sensing, the airborne polarimetric radar (POLSCAT) for ocean wind velocity measurements, the POLSCAT/Cold Land Processes Experiments (CLPX-1 and CLPX-2) in 2002–2004 and 2006–2008, the Advanced Component Technology lightweight dual-frequency antenna feed project, the Aquarius PALS High Wind Campaign in 2009, and the POLSCAT-CLPX-3 experiment in 2009–2010. He is the author of four book chapters and has published more than 150 publications and presentations.

Dr. Yueh received the 2009 IEEE GRSS Transaction Prize Paper Award, the 2002 IEEE GRSS Transaction Prize Paper Award, the 2000 Best Paper Award in the IEEE International Geoscience and Remote Symposium 2000, and the 1995 IEEE GRSS Transaction Prize Paper Award for a paper on polarimetric radiometry. He received the JPL Lew Allen Award in 1998 and Ed Stone Award in 2003. He is an Associate Editor of the IEEE TRANSACTIONS ON GEOSCIENCE AND REMOTE SENSING.



Wenqing Tang received the Ph.D. degree in physics from Michigan State University, East Lansing, MI, USA, in 1987.

In October 1989, she joined the Climate, Oceans and Solid Earth Section, Jet Propulsion Laboratory, California Institute of Technology, Pasadena, CA, USA. She has been working on scientific data analysis and retrieval algorithm development of satellite earth remote sensing data. She has been the Coinvestigator of many research projects, including the NASA Ocean Vector Wind Science Team on Sea-

Winds scatterometers NSCAT and QuikSCAT, the NASA Global Precipitation Measurement mission, and the NASA Energy and Water cycle Study. She was the Principal Investigator of the project producing global ocean surface vector wind fields and related geophysical parameters from space-based sensors under NOAA Climate and Global Change Program directed at climate change data and detection/enhanced data sets. She joined Aquarius Postlaunch Instrument Calibration and Validation Team in 2011, and she has been working on Aquarius radar/radiometer geophysical model functions and other research activities, including the rain effect on roughness correction to improve sea surface salinity retrieval.



Alexander G. Fore received the A.B. degree in physics from Vassar College, Poughkeepsie, NY, USA, in 2002 and the M.S. and Ph.D. degrees in physics from Carnegie Mellon University, Pittsburgh, PA, USA, in 2004 and 2008, respectively.

His doctoral work was modeling of complex fluids using the lattice Boltzmann method. In March 2008, he joined the Radar Science and Engineering Section, Jet Propulsion Laboratory, Pasadena, CA, USA, where he has been working primarily on scatterometry, both forward modeling of the radar observation

as well as retrieval of the geophysical quantity from the radar observation. He also has experience in synthetic aperture radar processing and calibration algorithms.



Simon H. Yueh (F'09) received the Ph.D. degree in electrical engineering from the Massachusetts Institute of Technology, Cambridge, MA, USA, in 1991.

He was a Postdoctoral Research Associate with the Massachusetts Institute of Technology from February to August 1991. In September 1991, he joined the Radar Science and Engineering Section, Jet Propulsion Laboratory (JPL), Pasadena, CA, USA. He was the Supervisor of the Radar System Engineering and Algorithm Development Group from 2002 to 2007. He was the Deputy Manager

of the Climate, Oceans and Solid Earth Section from July 2007 to March 2009 and the Section Manager from April 2009 to Jan 2013. He was also



Gregory Neumann received the M.S. degree in electrical engineering from Brigham Young University, Provo, UT, USA, in 1983.

He joined the Radar Science and Engineering Section, Jet Propulsion Laboratory, Pasadena, CA, USA, in 1984. He has contributed to several National Aeronautics and Space Administration (NASA) airborne and spaceborne radar missions. He was responsible for the deployment of a conical scanning Ku-band scatterometer (NUSCAT) on C-130 aircraft for ocean surface wind campaigns in the 1990s. He has worked

on system engineering of NASA Scatterometer flown on the Japanese Advanced Earth Observation Satellite, NASA SeaWinds Scatterometer on the QuikSCAT satellite, Shuttle Imaging Radar Mission (SRTM) for topographic measurements, and Aquarius mission for ocean surface salinity measurements. He is currently on the System Engineering Team for the integration and test of the L-band radar and radiometer for the NASA Soil Moisture Active–Passive mission.



Julian Chaubell received the B.S. degree from the University of Mar del Plata, Buenos Aires, Argentina, in 1997 and the Ph.D. degree in applied and computational mathematics from the California Institute of Technology, Pasadena, CA, USA, in 2004.

His doctoral work focused on low-coherence interferometric imaging. In April 2004, he joined the Jet Propulsion Laboratory (JPL), Pasadena, as a Postdoctoral Research Associate with the Tracking Systems and Applications Section, where he worked

on the modeling of EM wave propagation in fully 3-D atmospheric refractive index distributions. In April 2007, he joined the Radar Science and Engineering Section, JPL, as a permanent employee. He has been working on the forward modeling of radar and radiometer measurements as well as retrieval of the geophysical quantity from those measurements. He has also been working on electromagnetic modeling of electrically large aperture systems and structures.



Akiko Hayashi received the B.S. degree in civil engineering and the M.S. degree in structural engineering from Duke University, Durham, NC, USA.

She is a member of the Oceans and Ice Group, Jet Propulsion Laboratory (JPL), Pasadena, CA, USA. After graduating, she came to JPL to work in the Structures and Dynamics Technology Group, doing structural analysis and finite-element modeling. In 1988, she moved to the Oceanography Group, where she started working on altimetry data from GEOSAT. She is currently working on altimetry data from

OSTM/Jason-2 and ocean salinity data from Aquarius.



Adam Freedman received the B.S. degree in physics from Yale University, New Haven, CT, USA, in 1980 and the Ph.D. degree in marine geophysics from Massachusetts Institute of Technology, Cambridge, MA, USA, in 1987.

He joined the Technical Staff at the Jet Propulsion Laboratory, where he engaged in earth rotation studies until 1996. He then began working with the Radar Sciences Section, first on the GeoSAR airborne X- and P-band radar platform and then as Instrument System Engineer for the Aquarius Project. He now

is a System Engineer for the SMAP Mission.

Dr. Freedman is a member of the American Geophysical Union.



Gary S. E. Lagerloef received the Ph.D. degree in physical oceanography from the University of Washington, Seattle, WA, USA, in 1984.

He currently serves as a Principal Investigator of the NASA Aquarius Mission to study the interactions between the Earth's water cycle, ocean circulation, and climate. He has served on numerous science teams and working groups over the past 20 years, which include the Salinity Sea Ice Working Group (Chair), Satellite Altimeter Requirements for Climate Research Working Group (Cochair), NRC

Committee on Earth Gravity Measurements from Space, the AMS Committee on Sea Air Interaction and on NASA Science Working Teams for Topex/Poseidon/Jason missions, Ocean Vector Winds, and the Tropical Rainfall Measurement Mission. He has been a Guest Editor of the *Journal of Geophysical Research: Oceans* and is a member of several professional associations, learned, and technical societies. He is currently with Earth and Space Research, Seattle, WA, USA, which he cofounded in 1995. Prior to that, he was with Science Applications International Corporation and was the NASA Physical Oceanography Program Manager from 1988 to 1990. He has served in the NOAA Commissioned Officer Corps and in the U.S. Coast Guard. He is the author of over 60 publications and presentations. His research interests include ocean circulation and climate dynamics, with special emphasis on developing new applications for satellite remote sensing.